Journal of Catalysis **186,** 373–386 (1999)
Article ID jcat.1999.2568, available online at http://www.idealibrary.com on IDEAL®

A New Model Describing the Metal–Support Interaction in Noble Metal Catalysts

B. L. Mojet,*[,1] J. T. Miller,† D. E. Ramaker,‡ and D. C. Koningsberger*

*Department of Inorganic Chemistry and Catalysis, Debye Institute, Utrecht University, P.O. Box 80083, 3508 TB Utrecht, The Netherlands; †Amoco Research Center, E-1F, 150 West Warrenville Road, Naperville, Illinois 60563; and ‡Chemistry Department, George Washington University, Washington, DC 20052

Received February 15, 1999; revised May 17, 1999; accepted May 17, 1999

The catalytic activity and spectroscopic properties of supported noble metal catalysts are strongly influenced by the acidity/alkalinity of the support but are relatively independent of the metal (Pd or Pt) or the type of support (zeolite LTL or SiO_2). As the alkalinity of the support increases, the TOF of the metal particles for neopentane hydrogenolysis decreases. At the same time, there is a decrease in the XPS binding energy and a shift from linear to bridge bonded CO in the IR spectra. Analysis of the shape resonance in XANES spectra indicates that in the presence of chemisorbed hydrogen the difference in energy between the Pt–H antibonding orbital and the Fermi level decreases as the alkalinity of the support increases. Based on the results from the IR, XPS, and shape resonance data a new model is proposed in which the interaction between the metal and support leads to a shift in the energy of the metal valence orbitals. The EXAFS structural analysis indicates that the small metal particles are in contact only with the oxide ions of the support. Finally, a new spectroscopic characterisation, Atomic XAFS, is presented which provides new insights into the origin of the electronic changes in the metal. As the alkalinity of the support increases, there is decrease in the metal ionisation potential. The primary interaction is a Coulomb attraction between metal particle and support oxygen ions, which affects the metal interatomic potential. This model for the metal–support interaction explicitly excludes the need for electron transfer, and it can account for all observed changes in the catalytic, electronic, and structural properties of the supported metal particles induced by support acidity ranging from acidic to neutral to alkaline.

Key Words: **noble metal catalysts; metal–support interaction; neopentane hydrogenolysis; FTIR; XPS; XANES; shape resonance; AXAFS; new model.**

INTRODUCTION

Supported noble metal catalysts are used in a large number of commercially important processes, including (de)-hydrogenation, naphtha reforming, oxidation, and automotive exhaust catalysis (1). It is well known that the support influences the catalytic activity of the supported metal particles. Metals on acidic supports, such as H–Y, H–LTL, or SiO_2/Al_2O_3, have a higher hydrogenation and hydrogenolysis activity compared to metals on neutral or alkaline supports (2–6). Although the effect of support acidity/alkalinity on the catalytic properties of the supported metal particles is well established, the nature of this interaction remains unclear.

Generally, the changes in catalytic activity are ascribed to a modification of the electronic properties of the metal particles induced by a metal–support interaction, and several models have been proposed. One model suggests that the support protons are delocalised on the metal particle forming a proton adduct which withdraws electron density from the surface atoms (2). However, such proton adducts cannot account for an increase in electron density for metal particles on alkaline supports. Alternatively, it was proposed that with increasing support alkalinity, the electron density of the support oxygen atoms increases (2, 7, 8). Electron transfer between the support oxygen atoms and the nearby metal particles is thought to increase the electron density on the metal particles. These two models are similar in that both propose a transfer of electron density between the metal particles and the support. The difference between the models is that in the former the metal transfers electron density to the support protons, while in the latter the transfer occurs between the metal and the oxide ions.

A third explanation, based on theoretical calculations, suggested that the electron density in small metal particles is shifted toward nearby cations of the support (9, 10). The polarisation of electron density near the support surface leaves the metal atoms at the opposite surface electron deficient. According to this model, there is no net change in electron density of the metal cluster; however, the interaction with the support leads to lower electron density in the catalytically active surface atoms.

[1] Author to whom correspondence should be sent. Current address: Schuit Institute of Catalysis, Eindhoven University of Technology, P.O. Box 513, 5600 MB Eindhoven, The Netherlands. Fax: +31 40 245 5054. E-mail: B.L.Mojet@tue.nl.

0021-9517/99 $30.00

The present paper presents results on catalytic rates, EXAFS structural analysis, infrared data (IR), X-ray photoelectron spectroscopy (XPS), and hydrogen induced X-ray absorption near edge structure (XANES) shape resonance spectroscopy for Pt and Pd catalysts on zeolite and amorphous supports. Independent of the metal and type of support, the neopentane hydrogenolysis turnover frequency (TOF) decreases with increasing support alkalinity. The IR, XPS, and XANES shape resonance spectroscopies indicate that the changes in TOF are due to a metal–support interaction. Furthermore, these spectra indicate that these differences result from changes in the electronic properties of the metal particles. In addition, this paper reports on a new spectroscopic characterisation called "Atomic XAFS" (AXAFS) spectroscopy, providing insight in the nature of the metal–support interaction. The decrease in activity of metal clusters with increasing support alkalinity can be ascribed to a decrease in ionisation potential of the metal particles directly induced by the Coulomb potential of the support. This model for the metal–support interaction obviates the need for electron transfer, as suggested in other studies. Moreover, it can account for all observed changes in the catalytic, electronic, and structural properties of the supported metal particles induced by changes in composition of the support.

EXPERIMENTAL

Catalyst Preparation

The acidity/alkalinity of the LTL zeolite supports was varied by either impregnating a commercial K–LTL zeolite with KNO_3 or exchanging with NH_4NO_3 to give K/Al ratios ranging from 0.55 to 1.45 for Pd/LTL and 0.63 to 1.25 for Pt/LTL. Each LTL zeolite was calcined at 225°C. Palladium was added by incipient wetness impregnation using an aqueous solution of $(Pd(NH_3)_4)(NO_3)_2$, followed by drying at 125°C. For platinum the same procedure was applied by using $(Pt(NH_3)_4)(NO_3)_2$ followed by drying at 120°C. The catalysts are designated Pt/LTL(x) or Pd/LTL(x) with x representing the K/Al molar ratio.

The silica supports were prepared by ion-exchange of SiO_2 microspheres (Davison grade 644, 284 m^2/g, 1.12 cc/g) with increasing amounts of KOH followed by calcination at 400°C. Also, an acidic silica was prepared by ion-exchange of SiO_2 with excess of $Al(NO_3)_3$ followed by calcination at 400°C. Platinum was added by incipient wetness impregnation using an aqueous solution of $(Pt(NH_3)_4)(NO_3)_2$ followed by calcination at 225°C. The catalysts are designated Pt/SiO_2–X (*.**) with X representing Al or K and (*.**) the wt% of X.

The elemental analysis and chemisorption measurements were performed at Amoco Oil Laboratories. Chemisorption capacity was calculated based on the double isotherm technique. The catalysts were reduced at 400°C in H_2 and evacuated at 400°C, both for 1 h. The sample was cooled to room temperature *in vacuo* and the first adsorption isotherm was recorded. At room temperature, the sample was evacuated and a second isotherm was recorded. The chemisorption capacity was calculated as the difference between the two isotherms extrapolated to zero pressure. Dispersion was calculated based on the assumption that one CO atom (Pd/LTL) or H atom (Pt catalysts) adsorbed per metal surface atom. The results for all catalysts are given in Table 1.

TABLE 1

Elemental Analysis and Dispersion of Pd/LTL, Pt/LTL, and Pt/SiO_2

Catalyst[a]	Wt% Al	Wt% K	Wt% Pd or Pt	Dispersion (%)
Pd/LTL(0.55)	8.7	6.9	1.74	19.4[b]
Pd/LTL(1.01)	8.7	12.8	1.71	60.4[b]
Pd/LTL(1.45)	7.6	16.0	1.76	10.4[b]
Pt/LTL(0.63)	9.5	8.3	1.0	0.53[c]
Pt/LTL(0.96)	8.5	11.8	1.0	0.89[c]
Pt/LTL(1.25)	8.8	15.9	1.0	0.88[c]
Pt/SiO_2–Al(0.10)	0.10	—	1.54	0.60[c]
Pt/SiO_2	—	—	1.40	0.58[c]
Pt/SiO_2–K(0.39)	—	0.39	1.64	1.05[c]
Pt/SiO_2–K(0.77)	—	0.77	1.56	1.30[c]
Pt/SiO_2–K(1.14)	—	1.14	1.48	1.35[c]

[a] Value between brackets shows K/Al molar ratio.

[b] Determined by volumetric CO chemisorption, assuming 1 CO molecule per surface Pd atom.

[c] Determined by volumetric H_2 chemisorption, assuming 1 H atom per surface Pt atom.

Neopentane Hydrogenolysis

Neopentane hydrogenolysis was carried out for all catalysts in a fixed-bed reactor using 1.25 vol% neopentane in H_2 for Pd/LTL and 1.0 vol% neopentane in H_2 for Pt/LTL and Pt/SiO_2. The catalysts were prereduced in H_2 at the reaction temperature and conversion was adjusted between 0.5 and 2.0% by varying space velocity. The specific activity of Pd/LTL(1.45) was too low to measure at the same temperature as Pd/LTL(0.55). For this reason, the activities of Pd/LTL(1.01) and Pd/LTL(1.45) were determined at higher temperature and the activity of Pd/LTL(1.45) was estimated at lower temperature, assuming the ratios of activity are the same at low and high temperature. Further, for Pd/LTL also the conversion of propane (3.78 vol% propane in H_2) was determined. The initial turnover frequency (TOF) was determined by extrapolation to time zero. The TOF (at time zero) was calculated based on the dispersion values obtained by chemisorption (Table 1).

X-Ray Absorption Spectroscopy

The X-ray absorption spectra of the Pd K edge (Pd/LTL) and Pt L_3 edge (Pt/LTL and Pt/SiO_2) were taken at the SRS

(Daresbury) Wiggler Station 9.2, using a Si(220) double-crystal monochromator. The measurements were done in transmission mode using ion chambers filled with Ar to have an X-ray absorbance of 20% in the first ion chamber and of 80% in the second ion chamber. The monochromator was detuned to 50% maximum intensity to avoid higher harmonics present in the X-ray beam.

Samples were pressed into self-supporting wafers (calculated to have an absorbance of 2.5) and placed in a controlled atmosphere cell (11). The Pd/LTL catalysts were reduced in flowing hydrogen (purified and dried) at 300°C (heating rate 5°C/min) for 1 h. Subsequently, the samples were cooled under flowing He to avoid formation of palladium hydrides at lower temperatures, and spectra were taken at liquid nitrogen temperature. Pt/LTL and Pt/SiO_2 were reduced in flowing hydrogen at 300°C and cooled to liquid nitrogen temperature in hydrogen, where spectra were taken. In addition, spectra were also recorded at liquid nitrogen temperature for the Pt/LTL samples after reduction in H_2 at 300°C and subsequent treatment in flowing He for 1 h at 300°C to remove chemisorbed hydrogen (samples further denoted by He–Pt/LTL).

Standard procedures were used to extract the EXAFS data from the measured absorption spectra. The pre-edge background was approximated by a modified Victoreen curve, normalisation completed by dividing by the height of the absorption edge, and the background was subtracted using cubic spline routines (12). The EXAFS were analysed using the commercially available data-analysis package XDAP (13). The EXAFS data were fitted in *R-space* using phase and backscattering amplitudes directly obtained from experimental EXAFS data via Fourier filtering (14, 15). The fits were optimised by applying the difference file technique and using phase and amplitude corrected Fourier transforms (16).

XANES Shape Resonance

Recently, it has been shown that analysis of a shape resonance in the XANES spectra for noble metal catalysts gives direct information on the changes in the nature of the bonding between chemisorbed hydrogen and the metal cluster (17). The partially occupied platinum surface *d*-orbitals interact with the hydrogen 1*s* orbital producing bonding and antibonding Pt–H orbitals (18). As illustrated in Fig. 1, the Pt–H bonding orbital is localised more on the H atom, and the antibonding state (AS) is localised more on the surface Pt atoms. The bonding orbital is occupied; thus it is not visible by XAS. However, the empty antibonding orbital (AS) can be isolated by subtraction of the Pt L_3 and L_2 near-edge spectra with (i.e., Pt/LTL) and without chemisorbed hydrogen (i.e., He–Pt/LTL, see above). A full description has been given elsewhere (17). Briefly, both L_2 edges were aligned at 0.6 step height, whereas both the L_3 (Pt/LTL) and the L_3 (He–Pt/LTL) edges were aligned relative to the comparable L_2 edges with the help of the EXAFS oscillations relative to the L_2 edges.

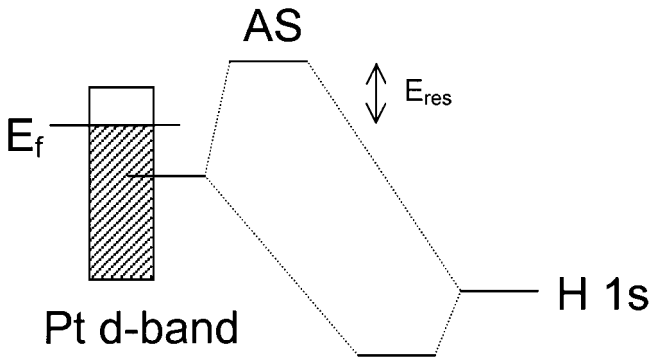

FIG. 1. MO-illustration of the formation of bonding and antibonding states from a surface Pt-orbital and an H 1*s* orbital (based on (18)).

This subtraction technique allows isolation of the antibonding state (AS) created by the chemisorption of hydrogen. This localised state is embedded in the continuum of the Pt metal cluster. Whenever a localised or bound state is degenerate with a continuum state, the well-known Fano-like spectra profile can be expected due to the auto-ionising probability of this state (19). The shape resonance can be described by the Fano expression, which enables a determination of the energy position of the antibonding state (E_{res}) relative to the Fermi level (17).

X-Ray Photoelectron Spectroscopy

X-ray photoelectron spectra of the Pd/LTL catalysts were measured using a VG ESCALAB-200 spectrometer with a monochromatic Mg $K\alpha$ X-ray source. Base pressure of the system was below 1.10^{-9} mbar. Energies were calibrated using the C 1*s* peak (284.6 eV), but peak positions did not change when the Si signal was used as a reference. The samples were reduced in flowing hydrogen at 300°C, followed by cooling under N_2 to avoid formation of palladium hydrides at lower temperatures. After reduction, the catalysts were ground under N_2 and pressed into indium foil to minimise charging effects during the XPS experiment. The reduced samples were transferred to the spectrometer under N_2 to prevent oxidation by air.

Infrared Spectroscopy

Transmission infrared spectra were recorded on a Perkin–Elmer 1720-X Fourier transform spectrometer at a spectral resolution of 4 cm^{-1}. The catalysts were pressed in thin self-supporting wafers and placed in an *in situ* transmission infrared cell provided with CaF_2 windows (11). Each catalyst was dried at 120°C, reduced in H_2 at 300°C, and cooled to room temperature under H_2 atmosphere, except

for Pd/LTL samples that were cooled in He to avoid formation of palladium hydrides. Subsequently at room temperature, the sample was purged with He for 10 min, followed by flowing 20% CO in He gas at atmospheric pressure for 10 min, after which the CO absorbance spectrum was collected at room temperature. The spectra for Pd/LTL and Pt/LTL were collected under wet conditions to prevent the ion–dipole interaction between zeolite cations and adsorbed CO (20). The spectra were corrected for the infrared adsorption of the specific support material and gas-phase CO.

ATOMIC XAFS SPECTROSCOPY

The principle of X-ray absorption is based on the photoelectron effect. Absorption of an X-ray photon results in the ejection of a core photoelectron which can be viewed as a spherical wave travelling outward, which can interfere with other nearby electron clouds. In general, an X-ray absorption spectrum can be described by $\mu = \mu_0(1 + \chi_{EX})$, μ being the total absorption, μ_0 being the absorption of an embedded (bound) atom, and χ_{EX} the EXAFS function. The EXAFS function contains information about the geometrical structure around the absorber atom for distances beyond the absorber atom itself. Fourier transformation of the experimental data results in a radial distribution function reflecting neighbouring atoms and distances. The physical origin of the EXAFS oscillations is the scattering of the outgoing photoelectron against the potential of neighbouring atoms, creating a back-scattered wave that interferes with the outgoing photoelectron (see Fig. 2a).

Interestingly, peaks are often observed in the Fourier transform at distances smaller than 1.5 Å from the absorber atom. These cannot be attributed to meaningful bond lengths with neighbouring atoms; rather, these distances point to a location inside the periphery of the absorber atom itself. In the raw data, these peaks show themselves as slowly varying sine waves. Rehr *et al.* attributed the low *R*-peaks in the Fourier transform to *Atomic* XAFS and gave a theoretical description of these low-frequency oscillatory phenomena (21). Atomic XAFS can be explained by scattering of the outgoing photoelectron against the atomic potential of the absorber atom itself (see Fig. 2a). Already in 1978, Holland *et al.* pointed out that μ_0 is not a smooth function but consists of an *atomic* absorption, μ_A, with an Atomic XAFS function given by $\mu_0 = \mu_A(1 + \chi_{AX})$ (22). Here, χ_{AX} arises from the change of the completely free atom to the embedded atom potential of the absorber atom.

Of crucial importance is that the AXAFS information can be extracted from the XAFS oscillations after an optimised procedure for background subtraction. Van Dorssen *et al.* (23) have shown that by application of this procedure the features due to the Ramsauer Townsend minimum and

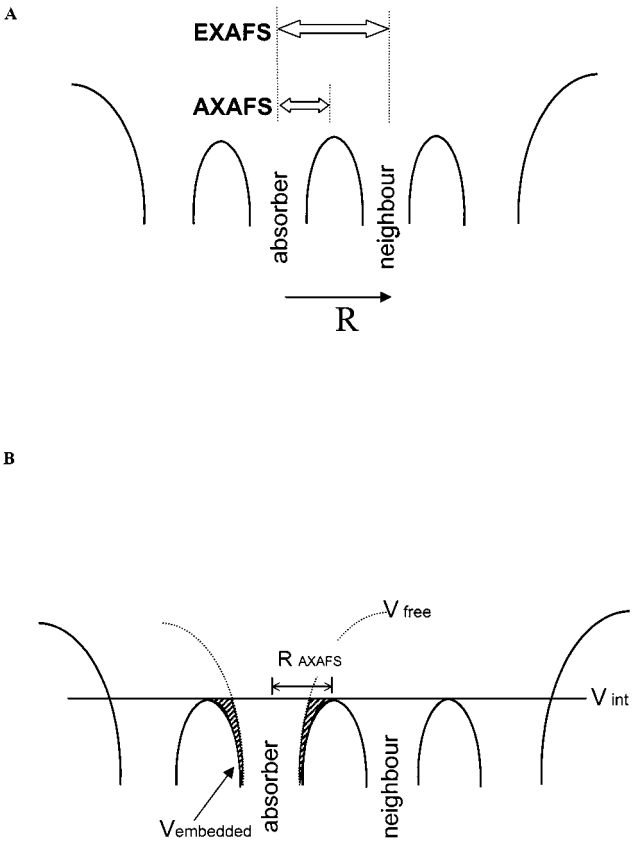

FIG. 2. (A) Atomic potential overlap: potentials responsible for AXAFS and EXAFS are indicated. (B) Intensity of the AXAFS peak in Fourier transform is proportional to V_{free} minus $V_{embedded}$ (shaded area). V_{int} represents the bottom of the conduction band in the muffin tin approximation.

multi-electron excitations are left in the background, implying that the AXAFS can be separated quantitatively from these contributions. In recently published papers (24–26) we have fully described the physical and chemical interpretation of AXAFS. It was shown that the Fourier transform of the AXAFS oscillations is proportional to the difference between the embedded potential V_e (i.e., an atom in a chemical environment) and the free atom potential. The shaded area in Fig. 2b represents this difference in atomic potentials and is proportional to the AXAFS peak in the Fourier transform. The position and intensity of the AXAFS peak can thus be used to derive direct information on the interatomic potential of the absorbing atom.

RESULTS

Neopentane Hydrogenolysis

Analysis of the reaction products, by the Delplot method (27) for neopentane conversions between 0.5 and 2.0%, indicated that the primary reaction products are methane, isobutane (hydrogenolysis), and isopentane (isomerisation), typical of a monofunctional metal catalysed reaction (28,

TABLE 2

TOF as Function of Support Acidity/Alkalinity

Catalyst	Neopentane TOF (mol/s surface metal atom)	Propane TOF (mol/s surface metal atom)
Pd/LTL(0.55)	5.7×10^{-3}	2.4×10^{0}
Pd/LTL(1.01)	1.3×10^{-4}	7.5×10^{-2}
Pd/LTL(1.45)[a]	8.1×10^{-7}	1.2×10^{-3}
Pt/LTL(0.63)	1.8×10^{-1}	—
Pt/LTL(0.96)	3.7×10^{-2}	—
Pt/LTL(1.25)	4.9×10^{-5}	—
Pt/SiO_2–Al(0.10)	3.1×10^{-2}	—
Pt/SiO_2	5.5×10^{-3}	—
Pt/SiO_2–K(0.39)	4.5×10^{-4}	—
Pt/SiO_2–K(0.77)	2.2×10^{-4}	—
Pt/SiO_2–K(1.14)	8.0×10^{-5}	—

Note. Pd/LTL: Neopentane TOF determined at 325°C, atmospheric pressure, and 1.25 vol% neopentane in H_2; propane TOF determined at 400°C, atmospheric pressure, and 3.78 vol% propane in H_2. Pt/LTL: Neopentane TOF determined at 350°C, atmospheric pressure, and 1.0 vol% neopentane in H_2. Pt/SiO_2: Neopentane TOF determined at 390°C, atmospheric pressure, and 1.0 vol% neopentane in H_2.

[a] TOF determined at 450°C and extrapolated to 325°C (neopentane) or 400°C (propane).

29). Table 2 reports the turnover frequencies (TOF) for neopentane or propane hydrogenolysis. For both zeolite and amorphous SiO_2 supported Pt and Pd, there is a continuous decrease in the TOF by 10^{-3} to 10^{-5} as the alkalinity of the support increases from acidic to neutral to alkaline.

EXAFS Structural Characterisation

Pd/LTL. Figure 3 shows the experimental EXAFS data for Pd/LTL(0.55), Pd/LTL(1.01), and Pd/LTL(1.45). The signal-to-noise ratio is excellent, which makes data analysis possible to 18 $Å^{-1}$. For example, the Fourier transform (k^1, 3.3–18.0 $Å^{-1}$) of the experimental data of Pd/LTL(0.55) is shown in Fig. 4a together with the best fit obtained by analysis in *R*-space (0.5–3.2 Å). The fit parameters of the model spectra are given in Table 3 together with the total variances. For all catalysts the imaginary and absolute

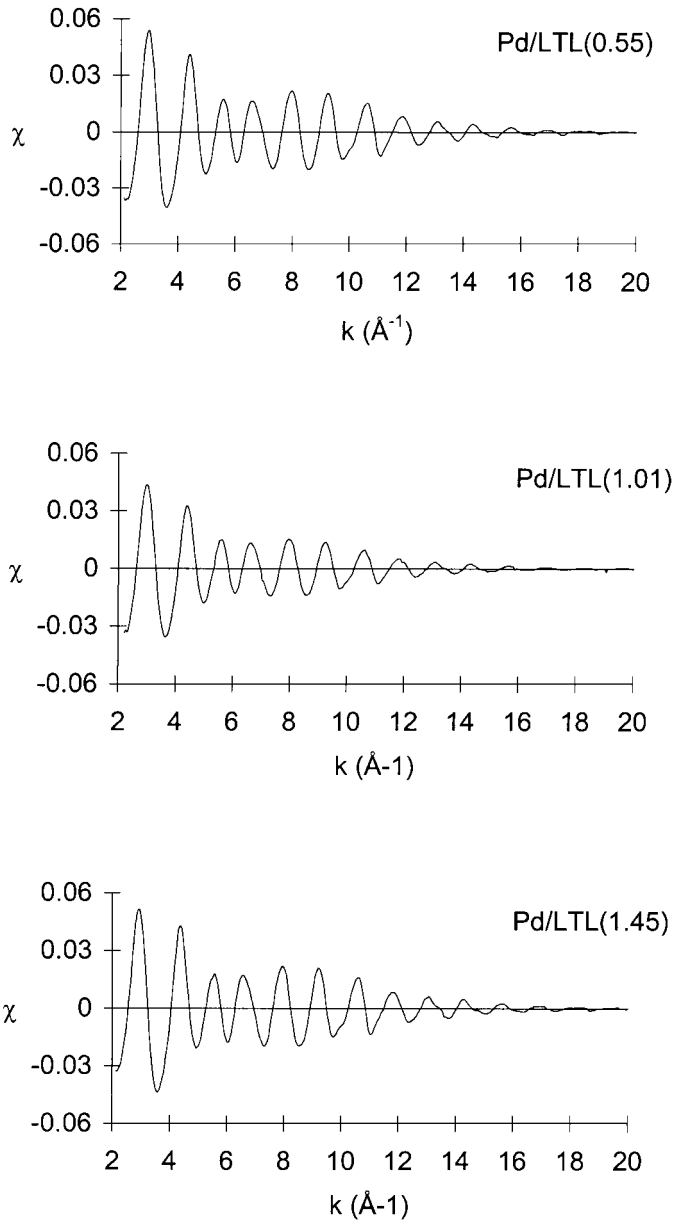

FIG. 3. Experimental EXAFS data of Pd/LTL catalysts.

TABLE 3

Fit Parameters of Pd/LTL EXAFS Spectra (Δk, 3.3–18 $Å^{-1}$; ΔR, 1.0–3.2 Å) and Variances of Fits

Catalyst	Scatterer	*N* (±5%)	*R* (Å) (±1%)	$\Delta\sigma^2$ (10^{-3} $Å^2$) (±5%)	ΔE_0 (eV) (±10%)	k^1-variance (%) Im.part	k^1-variance (%) Abs.part
Pd/LTL(0.55)	Pd	7.2	2.75	1.5	−1.4	0.2	0.1
	O	3.8	2.51	2.4	16.5		
Pd/LTL(1.01)	Pd	6.3	2.76	2.8	−2.1	0.3	0.2
	O	3.8	2.53	6.6	15.5		
Pd/LTL(1.45)	Pd	7.3	2.76	1.4	−0.5	0.2	0.1
	O	4.4	2.53	6.1	14.5		

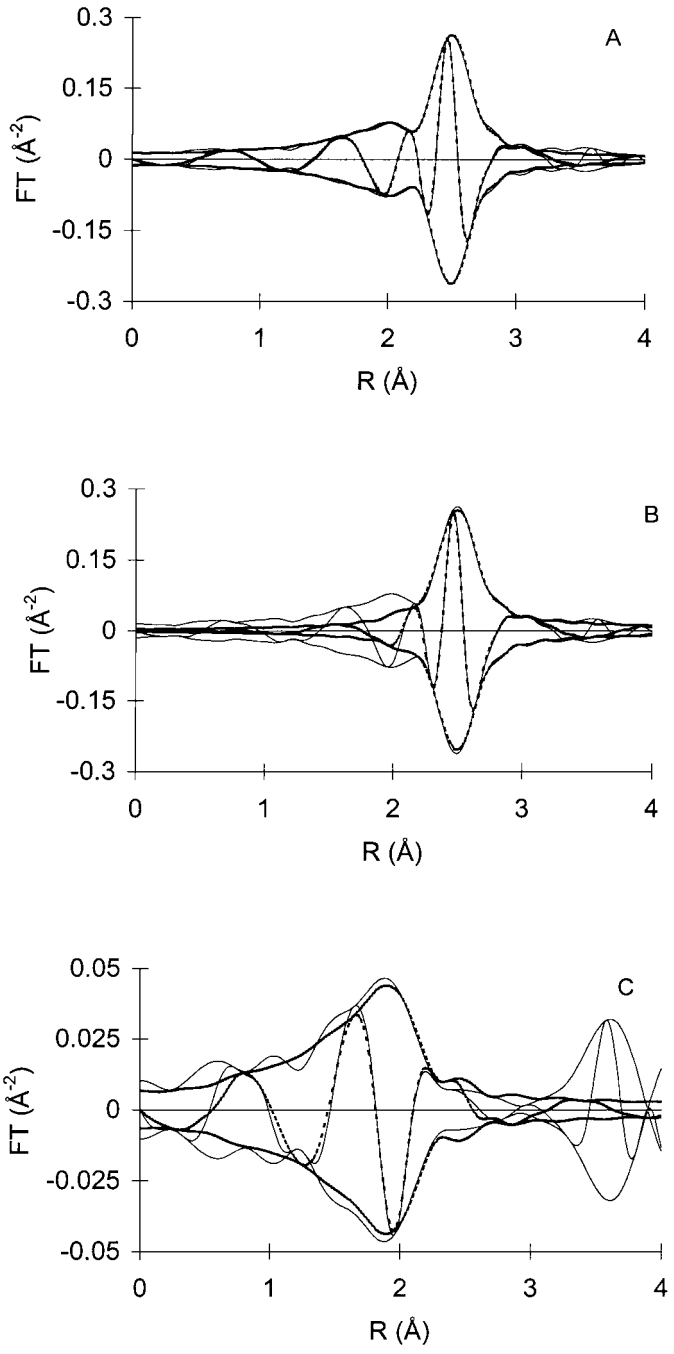

FIG. 4. Fourier transforms (k^1, 3.3–18 Å^{-1}) of experimental data, model spectra, and difference file of Pd/LTL(0.55). (A) Experimental data (solid line) and total fit (dotted line). (B) Experimental data (solid line) and calculated Pd–Pd contribution (dotted line). (C) Pd–O contribution, difference file: experimental data minus calculated Pd–Pd contribution (solid line) and calculated Pd–O contribution (dotted line).

parts of the model spectra are in good agreement with the Fourier transforms of the experimental data.

Figure 4b shows the Fourier transforms of Pd/LTL(0.55) which was fit with a first Pd–Pd coordination shell at 2.76 Å. The Pd–Pd distance is similar to the metal–metal distance in bulk palladium (2.74 Å). The Pd–Pd coordination numbers 6.3–7.3 correspond to metal particles that just fit inside the LTL pores. Assuming spherical metal particles with an FCC lattice, the average cluster size was calculated (30). A mean Pd–Pd coordination number of 7.2 (Pd/LTL(0.55) and Pd/LTL(1.45)) corresponds to a metal particle with a diameter of about 10 Å (43 atoms), and a coordination number of 6.3 (Pd/LTL(1.01)) corresponds to an average particle diameter of 8.5 Å (19 atoms).

An additional contribution between 1.0 and 2.2 Å was fit with a Pd–O coordination at 2.53 Å for all three catalysts. This Pd–O distance is similar to Pd-support distances as reported for palladium on carbon fibrils (15). The inner-potential corrections (ΔE_0) for the Pd–O scattering pair are around 15 eV, as shown in Table 3. This is due to the fact that PdO was used as a reference material. Both the Pd^{2+} oxidation state and coordination distance (2.03 Å) differ significantly from the experimental Pd^0–$O_{support}$ absorber–backscattering pair, resulting in large ΔE_0 values. Figure 4c shows the Fourier transforms of the experimental data of Pd/LTL (0.55) minus the first Pd–Pd model spectra (=difference file) together with the calculated Pd–O contribution. Both the amplitude and the imaginary part of the model are in good agreement with the experimental data between 1 and 2.5 Å. The peaks visible at distances >3 Å are due to second shell Pd–Pd scattering.

Remarkable is the high oxygen coordination number per palladium atom ($N \sim 4$). Commonly, metal–oxygen coordination numbers for small metal particles are between 1 and 2 (31, 32). However, as shown in Fig. 5, the 10 Å metal particles in Pd/LTL(0.55) and Pd/LTL(1.45) fit inside the pores of zeolite LTL, contacting the walls on all sides. This results in an average Pd–O coordination number of about 4, similar to Pd/LTL(1.01), even though the palladium clusters consist of twice as many atoms as those in Pd/LTL(1.01).

It can also be seen in Fig. 5 that because of the exact fit of the Pd particles in the zeolite pores, only a small fraction of the metal atoms (about 20%) are available for CO chemisorption. In addition, since the metal particles in Pd/LTL(1.01) do not completely fill the pore, there is a higher exposure of surface atoms. The lower dispersion of Pd/LTL(0.55) and Pd/LTL(1.45) compared to Pd/LTL(1.01) as determined by CO chemisorption (see Table 1) is consistent with the XAFS results. The dispersion for Pd/LTL(1.45) is also half of that for Pd/LTL(0.55), although the metal particles have similar coordination numbers. The FTIR spectroscopy of Pd/LTL(1.45), however, indicates that significantly more CO is chemisorbed in bridged coordination compared with Pd/LTL(0.55) (see below). The higher fraction of bridge bonded CO results in an underestimation of the dispersion by approximately a factor of two in Pd/LTL(1.45).

Pt/LTL and He–Pt/LTL. Details of the XAFS data and analysis of these samples are given elsewhere (17, 33). A

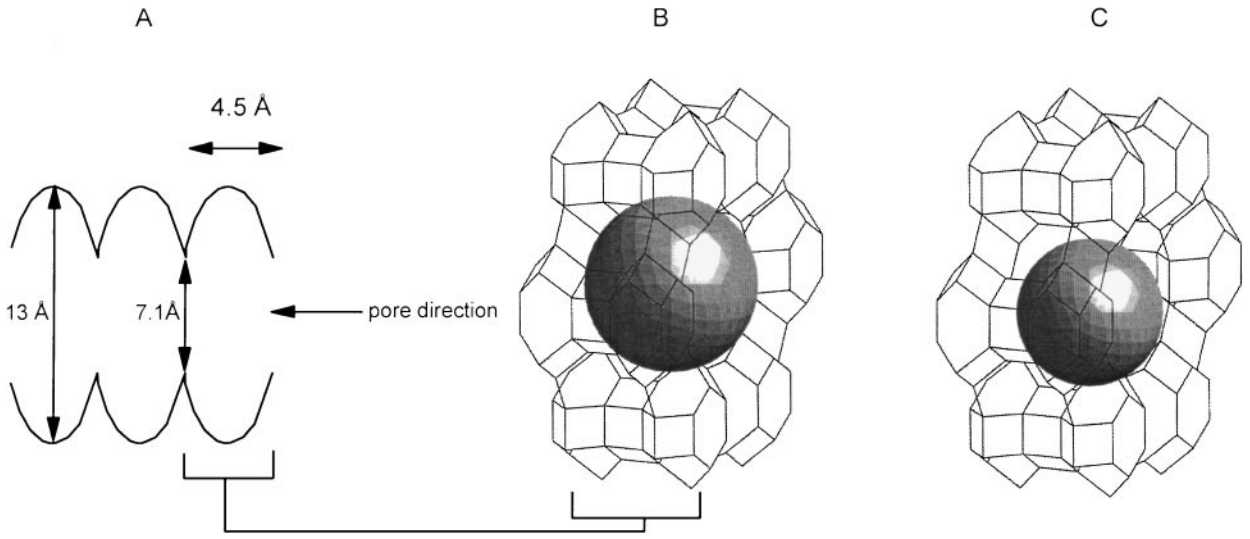

FIG. 5. Schematic picture of Pd particles inside zeolite LTL pore. (A) Pore diameters of zeolite LTL. (B) Metal particle of 10 Å in zeolite LTL pore. (C) Metal particle of 8.5 Å in zeolite LTL pore.

summary of the EXAFS parameters for the Pt/LTL samples is given in Table 4. It can be seen that the metal particles in the Pt/LTL series are very small with first shell Pt–Pt coordination numbers less than 4.5; i.e., the metal particles contain approximately 6 atoms on average. The long Pt–O distance of approximately 2.68 Å is in accordance with previous studies on Pt/LTL (34) and is generally attributed to the presence of interfacial hydrogen between the support and the metal particle. No potassium could be detected near the platinum particles.

Desorption of chemisorbed hydrogen by heating in flowing He at 300°C results in a slight contraction of Pt–Pt and Pt–O bond distances. For Pt/LTL(0.63), desorption of hydrogen leads to a short Pt–O distance at 2.26 Å. Previously, shorter Pt–O distances were reported upon evacuation of supported Pt catalysts at 300°C and were ascribed to loss of interfacial hydrogen. Apparently, with evacuation at 300°C more interfacial hydrogen desorbs than by heating in flowing He.

TABLE 4

Coordination Numbers and Distances Obtained for Pt/LTL and He–Pt/LTL (Δk, 3.2–14 Å^{-1}; ΔR, 1.8–3.1 Å) (17, 33)

Catalyst	Scatterer	N (±5%)	R (Å) (±1%)
Pt/LTL(0.63)	Pt	3.7	2.74
	O	2.1	2.69
Pt/LTL(0.96)	Pt	4.2	2.74
	O	1.6	2.69
Pt/LTL(1.25)[a]	Pt	2.3	2.72
	O	3.0	2.64
He–Pt/LTL(0.63)	Pt	4.2	2.72
	O	1.0	2.56
	O	0.3	2.26
He–Pt/LTL(0.96)	Pt	4.3	2.71
	O	1.1	2.58
He–Pt/LTL(1.25)	Pt	2.0	2.70
	O	1.3	2.61

[a] Here, Δk is 3.2–11.0 Å^{-1}, due to lower signal-to-noise ratio as only one spectrum was available.

Pt/SiO$_2$. Table 5 gives the fit parameters for the Pt/SiO$_2$ catalysts. The details of the XAFS data and analysis are described elsewhere (33). The Pt/SiO$_2$ catalysts have Pt–Pt coordination numbers between 5.3 and 7.6 and have metal particles comparable in size with those of the Pd/LTL catalysts. Each catalyst also exhibits a Pt–O contribution at a distance of 2.2 Å. No long Pt–O distance could be detected in these catalysts. The short Pt–O distance in the Pt/SiO$_2$ catalysts points to the absence of interfacial hydrogen which is in contrast to the long metal–oxygen distance previously reported in Pt/zeolite (29, 32), Ir/Al$_2$O$_3$ (32), and Pt/Al$_2$O$_3$ (14).

XPS of Pd/LTL

The Pd $3d_{5/2}$ and $3d_{3/2}$ XPS spectra are shown as a function of support acidity in Fig. 6. The palladium binding

TABLE 5

Coordination Numbers and Distances Obtained for Pt/SiO$_2$ (Δk, 3.2–14.8 Å^{-1}; ΔR, 1.6–3.1 Å) (33)

Catalyst	Scatterer	N (±5%)	R (Å) (±1%)
Pt/SiO$_2$–Al(0.10)	Pt	7.4	2.77
	O	0.5	2.23
Pt/SiO$_2$	Pt	7.7	2.77
	O	0.5	2.21
Pt/SiO$_2$–K(1.14)	Pt	5.3	2.77
	O	0.5	2.12

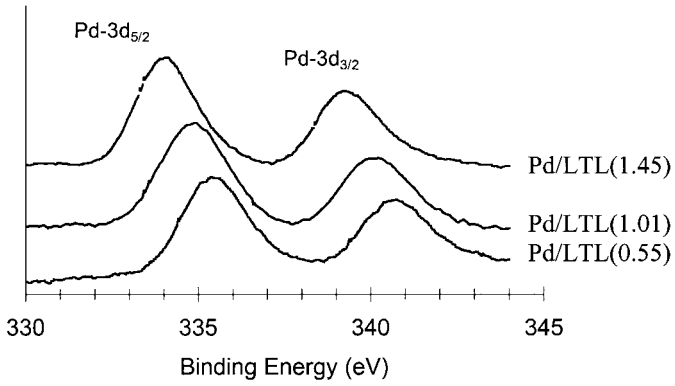

FIG. 6. Binding energy of Pd–3$d_{5/2}$ and Pd–3$d_{3/2}$ lines: Pd/LTL (0.55), dotted line; Pd/LTL(1.01), solid line; Pd/LTL(1.45), dashed-dotted line.

energies for Pd/LTL(1.01) were identical to those of palladium metal. The binding energy of Pd/LTL(0.55) was 0.6 eV higher, and that of Pd/LTL(1.45) was 0.8 eV lower than Pd on neutral LTL. These shifts indicate a gradual decrease in the binding energy with increasing support alkalinity.

In XPS, the binding energy has been shown to be particle size dependent, increasing by ca. 0.5 eV as the particle size is decreased from 50 to 10 Å (35). However, both TEM (not presented) and EXAFS analysis of the Pd/LTL catalysts indicated that the Pd particle sizes are similar. The change of 1.5 eV in binding energy (from acidic to alkaline) is much larger than can be accounted for by the small differences in particle size. Shifts to lower binding energy have also been reported in the literature for Pd/SiO_2 catalysts with increasing amounts of K_2O (36).

The XPS results can be interpreted as a change in electron density of the metal particles (electron deficient on acidic supports/electron rich on alkaline supports) or as a real lowering of the ionisation potential of the Pd valence orbitals with increasing alkalinity of the support. In either case, the XPS indicates that the interaction with the support induces a change in the electronic properties of the metal particles.

Infrared Spectroscopy

The transmission infrared spectra of the samples are displayed in Fig. 7, and are typical for Pd or Pt particles supported on zeolite LTL or SiO_2 (5, 6). Two regions of adsorbed CO can be assigned, at higher wavenumbers, an adsorption band due to linearly coordinated CO and at lower wavenumbers, adsorption due to CO in bridged coordination. Both adsorption bands shift to lower wavenumbers as the support alkalinity increases. Shifts in the CO band position are generally interpreted as evidence of changes in the electronic properties of supported metals. The exact position of the absorption bands depends on parameters such as particle size (37), surface coverage (38), and electronic changes in the metal structure (39). Since the particle sizes for a given catalyst series are not exactly the same and the bands are broad, the shifts in band position cannot only be interpreted as a change in electronic properties of the metal particles.

Theoretical calculations (40) have shown that the amount of bridged bonded CO increases at the expense of linear coordinated CO when the binding energy of the metal electrons is located closer (i.e., at lower binding energy) to the $2\pi^*$ orbital of CO. The integrated intensity ratios of the linear to bridged bonded CO (L/B ratio) calculated from the spectra in Fig. 7 are presented in Fig. 8. It can be seen that the L/B ratio decreases with increasing support alkalinity for all three catalyst series. When CO is coordinated in bridge position there is a better overlap between the metal *d*-orbitals and the CO-orbitals. If a metal particle has electron density at lower binding energy, it will have a larger backdonation towards CO due to the better overlap with the $2\pi^*$ orbital of CO. Consequently, CO will have a higher fraction of bridged bonded coordination. The integrated intensity ratio of linear/bridged bonded CO, therefore, is a direct measure of the overlap of the metal valence orbitals with the CO π^* orbitals.

XANES Shape Resonance of Pt/LTL

Figure 9 shows the shape resonance spectra for the Pt/LTL catalysts together with the model fit for a Fano shape resonance (dotted line). A full description of the data analysis has previously been given (17). Table 6 shows the energy position of the hydrogen-induced antibonding state relative to the Fermi level. There is a systematic decrease of the energy difference (E_{res}) between the Pt–H antibonding state and the Fermi level with increasing alkalinity of the LTL support. Since the energy of the H 1*s* orbital is constant, a change in the difference in energy between the Pt–H antibonding orbital and the valence *d*-orbitals implies that the energy of the metal valence orbital is affected by the support, i.e., decreasing with increasing alkalinity. A decrease in E_{res} also implies a weaker Pt–H bond and a decrease in the ionisation potential of the Pt *d*-orbitals.

Atomic XAFS of Pt/LTL

The Fourier transforms (k^3, Δk, 3–13 $Å^{-1}$) of the AXAFS oscillations of the Pt/LTL catalysts after desorption of chemisorbed hydrogen in He are shown in Fig. 10. As discussed above, the AXAFS peak position in the Fourier

TABLE 6

Resonance Energy of the Hydrogen-Induced Antibonding State (17)

Catalyst	E_{res} (eV) (± 0.3)
Pt/LTL(0.63)	2.0
Pt/LTL(0.96)	1.1
Pt/LTL(1.25)	−1.2

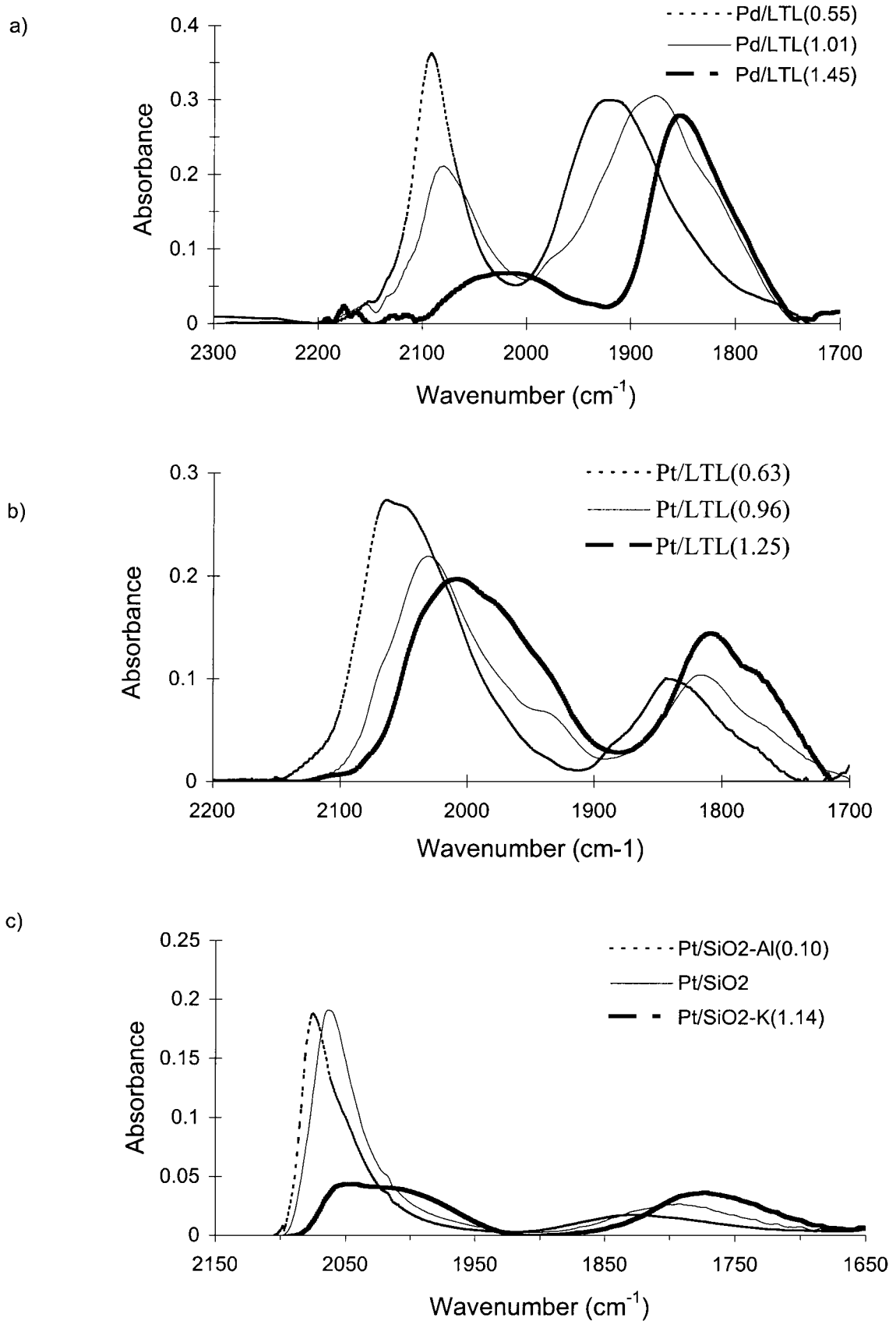

FIG. 7. Transmission FT-IR spectra of adsorbed CO: (a) Pd/LTL, (b) Pt/LTL, (c) Pt/SiO_2.

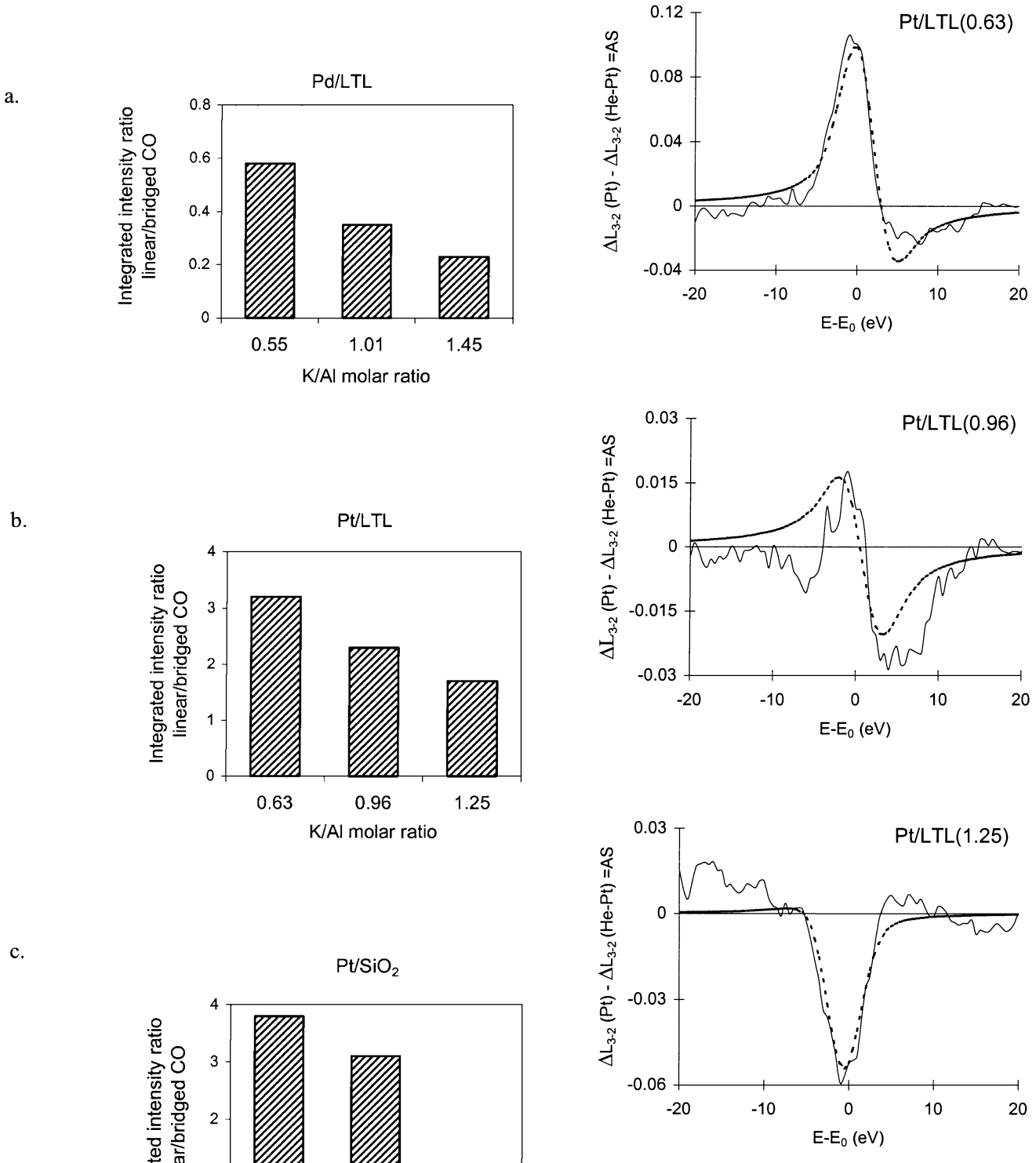

FIG. 8. Integrated intensity ratio of linear/bridged CO as a function of support acidity/alkalinity for Pd/LTL, Pt/LTL, and Pt/SiO_2.

FIG. 9. XANES shape resonance for Pt/LTL (solid line) and best fit to resonant line shape (dotted line).

transform is at low *R*-values (around 0.8 Å, uncorrected Fourier transform) and is expected to be at the periphery of the X-ray absorbing platinum atom. The peak position shifts to longer *R*-values with increasing support alkalinity.

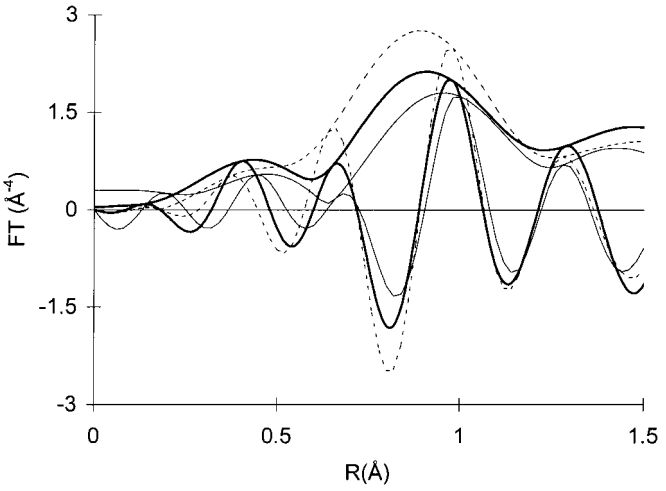

FIG. 10. AXAFS spectra (FT, k^3, $\Delta k = 3$–13 Å^{-1}) of He–Pt/LTL catalysts. Pt/LTL(0.63), dotted line; Pt/LTL(0.96), solid line; Pt/LTL(1.25), thin solid line.

At the same time, the amplitude of the AXAFS peak systematically decreases. Better separation of the AXAFS from the EXAFS oscillations can be obtained by substracting fits of the first shell Pt–Pt and Pt–O contributions from the experimental EXAFS data. However, this does not change the observed trends in intensity and peak position in the AXAFS.

DISCUSSION

Catalytic Activity

The hydrogenolysis activity of palladium or platinum on LTL zeolite decreases as the composition of the support changes from acidic to neutral to alkaline, which is in agreement with hydrogenolysis TOF of neopentane (3–6, 41, 42) and propane (4–6, 43) reported in the literature. Further, the lower TOF of propane on Pd/LTL(1.45) indicates that the lower activity is not due to pore-blocking by alkali but results from a change in metal activity. FTIR spectroscopy indicates there is a shift from linear to bridge bonding as the alkalinity of the support increases, which introduces an inaccuracy in the number of surface sites determined by CO chemisorption. The maximum error in the number of surface sites is about a factor of two. The observed changes in catalytic activity, however, differ by several orders of magnitude and, therefore, are not due to the uncertainty in the number of Pd surface atoms.

For the Pt/SiO_2 catalysts, the effect of increasing support alkalinity on the catalytic activity is similar to that for Pd and Pt on LTL zeolite. There is a continuous decline in TOF with increasing support alkalinity from acidic to neutral to alkaline supports, suggesting that the metal–support interaction is similar in nature for all catalysts.

Changes in Metal Valence Orbital Energy

Figure 11 shows the Ln (TOF) versus Pd $3d_{5/2}$ binding energy for Pd/LTL. The linear correlation between catalytic activity and binding energy for both neopentane and propane implies that the changes in the catalytic rate are due to the changes in the electronic properties of the metal particles induced by the acidity/alkalinity of the support.

Figure 8 reveals a decreasing L/B ratio with higher support alkalinity for all catalysts. It can be concluded that the electron density of the surface metal atoms shifts to lower binding energy with increasing alkalinity of the support, forcing the CO molecules to be bonded in bridged position. These results indicate that the metal–support interaction leads to a shift in the ionisation potential of the metal valence orbitals, consistent with the interpretation of the XPS data. The correlation between the catalytic activity and the L/B ratio again implies that the changes in rate are due to alterations in the electronic properties of the metal particles due to an interaction with the support.

Finally, the XANES shape resonance analysis shows that the hydrogen-induced antibonding state is located closer to the Fermi level with increasing support alkalinity. The interpretation of the shape resonance analysis is in agreement with the more classical IR and XPS techniques and supports the proposal that the acidity/alkalinity of the support affects the energy of the valence orbitals. Figure 12 gives an overview of the effect of increasing support alkalinity on the valence orbitals as deduced from XPS, FTIR, and XANES shape resonance data.

While IR, XPS, and the XANES shape resonance provide evidence that the support composition leads to a change in the energy of the metal valence orbitals, these techniques do not give information about the mechanism by which the support alters the electronic properties of the metal particles. Insight into the origin of the metal–support interaction,

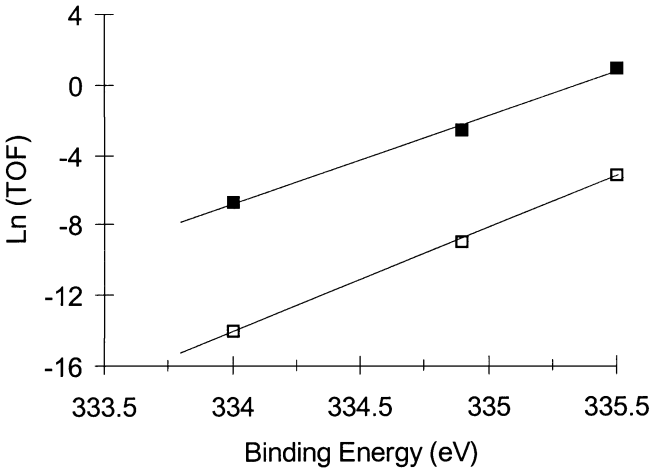

FIG. 11. Correlation between Pd–$3d_{5/2}$ binding energy and Ln (TOF) for neopentane, open squares, and propane hydrogenolysis, closed squares.

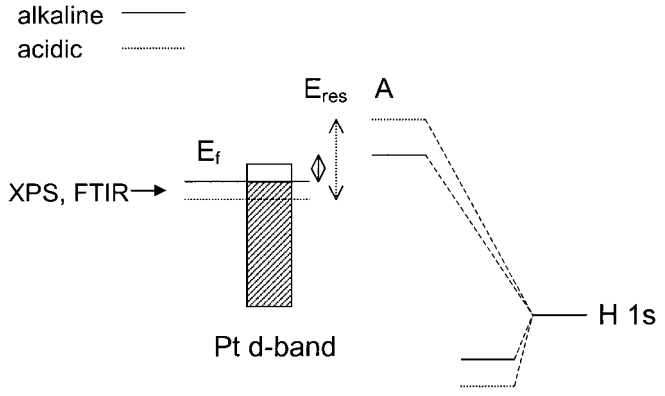

FIG. 12. Schematic representation of the change in Pt–H bonding and metal valence orbitals as a function of support acidity/alkalinity.

however, can be obtained by Atomic XAFS. In Fig. 10 it can be seen that the position and intensity of the AXAFS peaks differ for each catalyst, again indicating that the support composition affects the electronic properties of the metal particles. The combination of a change in position and intensity of the AXAFS provides new information on the exact nature of the alteration of the electronic structure.

As explained in Fig. 2, the AXAFS intensity and position are related to the difference between the free atom potential and the interatomic metal potential. The interatomic potential of the platinum atoms close to the support will be most strongly influenced by nearby atoms, which are the oxide ions of the support, as shown by EXAFS analysis. The Coulomb potential field of the support oxygen ions will extend to the metal and will lead to a change in the shape of the metal atomic potential. This results in a larger "rollover" of the interatomic potential compared to an isolated (unsupported) metal particle. By increasing the negative charge on the support oxygen (as in alkaline supports) the interatomic potential between platinum and oxygen will move up (moves to lower binding energy and becomes less attractive), resulting in less "rollover" as schematically shown in Fig. 13.

In Fig. 13, the total metal electron density is unchanged. V_{int} represents the bottom of the conduction band in the muffin tin approximation, and the shaded area represents the difference between the embedded (supported) potential (V_e) and the free atom (isolated) potential truncated by V_{int}. Since the experimental AXAFS peak intensity decreases with alkalinity, it can be concluded that with higher support alkalinity the difference between the supported and isolated potential decreases. In other words, the smaller difference results from a weaker attractive interaction between the support oxygen and the Pt potential.

Further, as the supported Pt potential decreases, V_{int} (the bottom of the conduction band) must move to lower binding energy as well (see Fig. 13). This causes the position of the weighted average of the shaded area (indicated with a vertical line) to move to larger R with increasing alkalinity, in agreement with the experimentally observed change of the position of the AXAFS peak. Finally, with the total metal electron density unchanged, the electron density distribution moves to lower binding energy when the alkalinity increases, consistent with the XPS, IR, and XANES shape resonance results.

A New Model Describing the Metal–Support Interaction in Noble Metal Catalysts

Many models have been previously suggested to account for the observed changes in metal electron density distribution as a function of support acidity/alkalinity. However, none of these can explain all observations from acidic to neutral to alkaline supports. The formation of metal–proton adducts was suggested to explain "electron-deficient" palladium particles on acidic zeolite supports (3, 42). However, the continuous shift in catalytic and electronic properties of the metal as the supports becomes more alkaline, where acidic hydroxyls are not present, indicates that the change in metal properties cannot be attributed solely to interaction with acidic hydroxyls.

Further, XPS, XANES shape resonance, and AXAFS data show that the average electronic structure of the metal particles is affected by the metal–support interaction, since these techniques probe all atoms in the small particles. For this reason, the observed changes cannot be attributed to a simple polarisation or redistribution of the electron charge

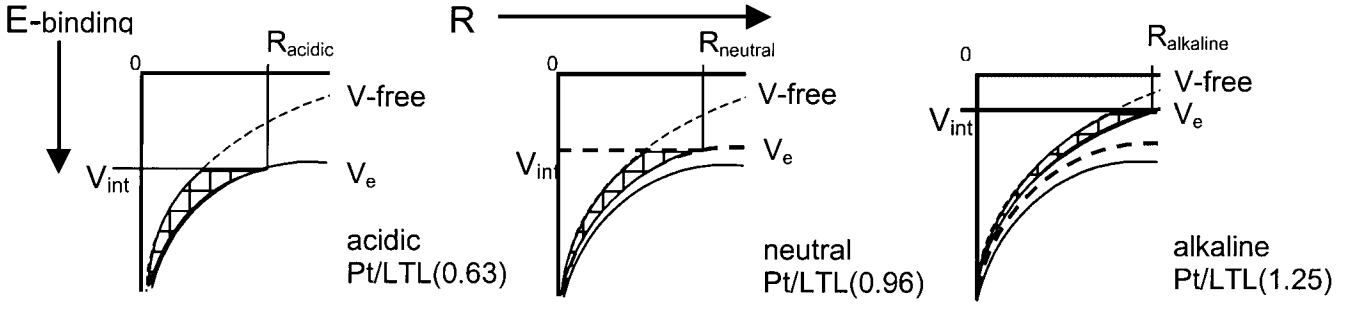

FIG. 13. Schematic illustration of interatomic potential changes in Pt/LTL catalysts as a function of support acidity/alkalinity.

inside the cluster induced by a nearby cation (9, 10). This kind of polarisation, although distorting the electron density inside the metal particle, leaves the average binding energy (XPS) and potential difference (AXAFS) the same.

Charge transfer between support oxygen atoms and the nearby metal particles actually increases the electron density of the metal particles (2, 7, 8). However, since the support material is an insulator, electron transfer to or from the support is unlikely. Moreover, if there were an actual electron transfer, the AXAFS intensities would change differently from what is observed. Recently, it was shown that an increasing number of electrons in the Pt valence orbitals also decreases the AXAFS intensity but without a change in shape or position (distance) (44).

A combined interpretation of the catalytic activity, EXAFS structural analysis, XPS, FTIR of chemisorbed CO, XANES shape resonance, and AXAFS leads to a new model describing the nature of the metal–support interaction in supported noble metal catalysts. The model is based on the change in the energy position of the metal valence orbitals as a result of the metal–support interaction, a decrease of the metal ionisation potential with increasing alkalinity. The primary interaction is a Coulomb attraction between the metal particle and support oxygen ions; this affects the interatomic potential, as clearly observed by AXAFS spectroscopy. This new model obviates the need for electron transfer and is able to explain all observed changes in catalytic and electronic properties of the catalysts.

CONCLUSION

The nature of the metal–support interaction that affects the electronic properties of supported noble metal catalysts, and in turn changes the catalytic activity, has been elucidated. As the alkalinity of the support increases, there is a decrease in the metal ionisation potential, i.e., a shift to lower binding energy due to the electrostatic Coulomb interaction between the support material and metal particle. A decrease in the ionisation potential of the metal valence orbitals with increasing support alkalinity can also account for all the changes observed in the IR, XPS, and XANES shape resonance data. In addition, as demonstrated by the XANES shape resonance of chemisorbed hydrogen, the changes in energy of the metal valence orbitals alter the chemisorption energy. These changes in the chemisorption energy between the metal and adsorbate directly influence the catalytic rate. Further studies are in progress (45) to more fully explore the AXAFS technique and, in addition, verify this new model.

REFERENCES

1. "Oil and Gas Journal Data Book." Penn Well, Tulsa, 1994.
2. Larsen, G., and Haller, G. L., *Catal. Lett.* **3**, 103 (1989).
3. Karpinski, Z., Gandhi, S. N., and Sachtler, W. H. M., *J. Catal.* **141**, 337 (1993).
4. Miller, J. T., Modica, F. S., Meyers, B. L., and Koningsberger, D. C., *Prep. ACS Div. Petr. Chem.* **38**, 825 (1993).
5. Mojet, B. L., Kappers, M. J., Miller, J. T., and Koningsberger, D. C., *Stud. Surf. Sci. Catal.* **101**, 1165 (1996).
6. Mojet, B. L., Kappers, M. J., Muijsers, J. C., Niemantsverdriet, J. W., Miller, J. T., Modica, F. S., and Koningsberger, D. C., *Stud. Surf. Sci. Catal.* **84**, 909 (1994).
7. de Mallmann, A., and Barthomeuf, D., *J. Chim. Phys.* **87**, 535 (1990).
8. Sugimoto, M., Katsuno, H., Hayasaka, T., Ishikawa, N., and Hirasawa, K., *Appl. Catal. A General* **102**, 167 (1993).
9. Jansen, A. P. J., and van Santen, R. A., *J. Phys. Chem.* **94**, 6764 (1990).
10. Sanchez-Marcos, E., Jansen, A. P. J., and van Santen, R. A., *Chem. Phys. Lett.* **167**, 399 (1990).
11. Vaarkamp, M., Mojet, B. L., Modica, F. S., Miller, J. T., and Koningsberger, D. C., *J. Phys. Chem.* **99**(43), 16067 (1995).
12. Cook, J. W., Jr., and Sayers, D. E., *J. Appl. Phys.* **52**, 5024 (1981).
13. Vaarkamp, M., Linders, J. C., and Koningsberger, D. C., *Physica B* **208–209**, 159 (1995).
14. Vaarkamp, M., Miller, J. T., Modica, F. S., and Koningsberger, D. C., *J. Catal.* **163**, 294 (1996).
15. Mojet, B. L., Hoogenraad, M. S., van Dillen, A. J., Geus, J. W., and Koningsberger, D. C., *J. Chem. Soc. Faraday Trans.* **93**(24), 4371 (1997).
16. Koningsberger, D. C., *in* "Applications to Solid State Physics and Chemistry" (J. Baruchel, J. L. Hodeau, M. S. Lehmann, J. R. Regnard, and C. Schlenker, Eds.), Neutron and Synchrotron Radiation for Condensed Matter Studies, Vol. II., p. 213. Springer-Verlag, Berlin/New York, 1994.
17. Ramaker, D. E., Mojet, B. L., Garriga Oostenbrink, M. T., Miller, J. T., and Koningsberger, D. C., *Phys. Chem. Chem. Phys.* **1**, 2293 (1999).
18. Hammer, B., and Nørskov, J. K., *Nature* **376**, 238 (1995).
19. Taylor, J. R., "Scattering Theory: The Quantum Theory of Nonrelativistic Collisions," p. 243. Krieger, Melbourne, FL, 1983.
20. Kappers, M. J., Vaarkamp, M., Miller, J. T., Modica, F. S., Barr, M. K., van der Maas, J. H., and Koningsberger, D. C., *Catal. Lett.* **21**, 235 (1993).
21. Rehr, J. J., Booth, C. H., Bridges, F., and Zabinsky, S. I., *Phys. Rev. B* **49**, 12347 (1994).
22. Holland, B. W., Pendry, J. B., Pettifer, R. F., and Bordas, J., *J. Phys. C Solid State Phys.* **11**, 633 (1978).
23. Van Dorssen, G. E., Koningsberger, D. C., and Ramaker, D. E., submitted.
24. Ramaker, D. E., Mojet, B. L., Koningsberger, D. C., and O'Grady, W. E., *J. Phys. Condens. Matter* **10**, 8753 (1998).
25. Ramaker, D. E., Qian, X., and O'Grady, W. E., *Chem. Phys. Lett.* **299**, 221 (1998).
26. Ramaker, D. E., Mojet, B. L., and Koningsberger, D. C., *J. Sync. Rad.*, in press.
27. Bhore, N. A., Klein, M. T., and Bischoff, K. B., *Ind. Eng. Chem. Res.* **29**, 313 (1990).
28. Anderson, J. R., and Avery, N. R., *J. Catal.* **7**, 315 (1967).
29. Davis, S. M., and Somorjai, G. A., *in* "The Chemical Physics of Solid Surfaces and Heterogeneous Catalysis" (D. A. King and D. P. Woodruff, Eds.), Vol. 4. Elsevier, Amsterdam, 1982.
30. Voogt, E. H., "Numie Software." Debye Institute, Utrecht University, Utrecht, 1996.
31. Vaarkamp, M., Modica, F. S., Miller, J. T., and Koningsberger, D. C., *J. Catal.* **143**, 395 (1993).
32. van Zon, F. B. M., Maloney, S. D., Gates, B. C., and Koningsberger, D. C., *J. Am. Chem. Soc.* **115**, 10317 (1993).
33. Mojet, B. L., Miller, J. T., and Koningsberger, D. C., *J. Phys. Chem. B* **103**(14), 2724 (1999).

34. Vaarkamp, M., Modica, F. S., Miller, J. T., and Koningsberger, D. C., *J. Catal.* **144**, 611 (1993).
35. Nosova, L. V., Stenin, M. V., Nogin, Yu. N., and Ryndin, Yu. A., *Appl. Surf. Sci.* **55**, 43 (1992).
36. Pitchon, V., Guenin, M., and Praliaud, H., *Appl. Catal.* **63**, 333 (1990).
37. van Hardeveld, R., and Hartog, F., *Adv. Catal.* **22**, 75 (1972).
38. Stoop, F., Toolenaar, F. J. C. M., and Ponec, V., *J. Catal.* **73**, 50 (1982).
39. Blyholder, G., *J. Phys. Chem.* **68**, 2772 (1964).
40. van Santen, R. A., *J. Chem. Soc. Faraday Trans. I* **83**, 1915 (1987).
41. Dalla Betta, R. A., and Boudart, M., *in* "Proceedings, 5th International Congress on Catalysis, Palm Beach, 1972" (J. W. Hightower, Ed.), Vol. 2, p. 1329. North Holland, Amsterdam, 1973.
42. Homeyer, S. T., Karpinski, Z., and Sachtler, W. M. H., *J. Catal.* **123**, 60 (1990).
43. Vaarkamp, M., Miller, J. T., Modica, F. S., Lane, G. S., and Koningsberger, D. C., *in* "Proceedings, 10th International Congress on Catalysis, Budapest, 1992" (L. Guczi, F. Solymosi, and P. Tetenyi, Eds.), p. 809. Akadémiai Kiadó, Budapest, 1993.
44. O'Grady, W. E., and Ramaker, D. E., *Electrochim. Acta* **44**(8–9), 1283 (1998).
45. Ramaker, D. E., Mojet, B. L., and Koningsberger, D. C., submitted.